Numerical investigation of a Hall thruster plume: domain size, boundary conditions, cathode location

A. Domínguez-Vázquez,[1, a)] J. Zhou,[2] A. Sevillano-González,[2] and E. Ahedo[2]
[1)] *Universidad de Málaga, 29071 Campanillas, Spain*
[2)] *Universidad Carlos III de Madrid, 28911 Leganés, Spain*

(Dated: 15 June 2025)

The current-free expanding plasma beam from a Hall effect thruster with a lateral hollow cathode is investigated through a 2D axisymmetric hybrid particle-in-cell/fluid code. A new model imposing a global zero current condition at the plume downstream boundary is presented. This work presents a new model that summarizes the global neutralization of the ejected ion beam at the far-field plume into a net zero-current condition, which is imposed at the downstream plume boundary of the simulation domain. This model outperforms the common local zero current condition, as it provides an estimation of the final potential of the plume and limits electron detachment from the magnetic lines induced by the plume boundary. Effects of plume size and cathode position on the plasma current solution in the plume and the coupling between cathode electrons and the ion beam are assessed for the two plume conditions. The new model provides a more robust current solution in the plume against plume truncation, especially when the externally-mounted cathode is outside the magnetic separatrix. This increases the reliability of the results for smaller, less computationally demanding plume domains, and is of central importance for validation of simulation results against experimental data from plume diagnostics. Compared to the operation with an externally-mounted cathode, positioned both inside and outside the magnetic separatrix, the discharge performance is enhanced for a centrally-mounted cathode due to the improved cathode-beam coupling, consistent with previous experimental and numerical studies.

I. INTRODUCTION

In the near plume of a Hall effect thruster (HET) complex physical processes take place that remain not fully understood, and which play an important role in thruster performances and its integration with other spacecraft systems. Specifically, the neutralization of the expanding plasma jet and the interaction between the ion beam and the electron flow emitted from the neutralizer cathode are influenced by several factors, including the cathode's position[1–6], its relative placement within the magnetic configuration[7–10], and the electrical setup of the testing facilities[11–14]. Consequently, progress towards the development of an accurate and predictive model for the near plume of a HET is of significant importance.

Many hybrid models, implementing a particle-in-cell (PIC) formulation for heavy species (ions and neutrals) and a fluid model for electrons[15–21], and multi-fluid[22–24] models used in HET research typically simulate the plasma discharge inside the thruster channel and in a limited plume region. Simulating large plumes is computationally expensive and plume truncation is unavoidable. However, for a precise characterization of the discharge performance, simulations must include a sufficiently large portion of the plume. Effects of plume truncation on the numerical solution and, in particular, uncertainties on appropriate boundary conditions to be applied at the outflow boundary, hinder the validation of simulation models against experimental data from plasma diagnostics in the near plume. Therefore, setting appropriate boundary conditions at the downstream plume boundary of the finite simulation domain is of central importance. These must be consistent with the global neutralization of the electric current in the far plume and the decay of the electric potential towards a uniform downstream value, representing either the infinity of free space or the metallic walls of a large vacuum chamber.

A widely adopted, although somewhat limiting, approach is the application of a local plume condition (LPC), which sets the plasma current to zero locally, i.e., at any point along the plume boundary[17,20,22]. While straightforward to implement, this assumption may only be valid for sufficiently large plumes and could introduce may lead to numerical errors if the truncated plume simulated is too small. For instance, Ref. 25 noted that H6 thruster multi-fluid simulations required to place the downstream boundary at a distance of at least 10 channel lengths downstream the thruster exit plane to avoid artificially increased electron transport across magnetic lines due to the zero local current condition. Moreover, the LPC model gives no information about the final potential in the plume nor the electron energy flux through the plume boundary. Previous numerical studies with multi-fluid[22,26] and hybrid[17,27] models set the electron temperature at the plume boundary. In Ref. 26 it is found that the temperature solution in the near field (from about three channel lengths downstream the thruster exit) is largely driven by the prescribed boundary value, which is informed from plasma measurements. Therefore, to be consistent, this approach requires accurate electron temperature measurements in the plume, which may be only available for a limited range of operational conditions.

[a)] Electronic mail: adoming@uma.es

The first goal of this paper is to present a global plume condition (GPC) model, which enforces a net current-free condition at the plume boundary, while locally decoupling ion and electron currents there. Unlike the LPC model, the GPC model allows for the estimation of the final potential of the plume at infinity and provides an expression for the electron energy flux at the plume boundary. The second, complementary goal here is to evaluate the robustness of the plasma solution in the near plume region with respect to plume size for both the GPC and LPC models. For that purpose, four different plume sizes will be considered.

Finally, the third goal of this paper is to analyze the influence of the cathode position on the neutralization of the ion beam current emitted by the thruster through the electron flow emitted from the cathode, as well as the coupling voltage required for this process. In the near plume of HET with a conventional (i.e., non-shielded) magnetic topology, an off-axis magnetic separatrix (MS) surface typically exists, which separates closed and open magnetic field lines. Several experimental studies have shown a significant impact on performance and plasma variables when the externally-mounted (i.e., off-axis) cathode is positioned either inside or outside the MS[7–10]. These two cases will be analyzed here. The magnetic field line passing through the center of the cathode injection surface will be referred to as the cathode magnetic line (CML), and it guides the trajectory of the central portion of the emitted magnetized electron beam. When the cathode is placed inside the MS, the CML forms a closed loop within the near plume. In contrast, when the cathode is positioned outside the MS, the CML extends farther downstream and intersects the boundary of the truncated plume. In this case, the plasma behavior in the plume is expected to be more influenced by the size and boundary of the plume. On the other hand, other experimental[2,4] and numerical[28,29] studies have compared the operation with externally and centrally-mounted (i.e., on-axis) cathodes, and have reported lower plume divergence and higher efficiency when the cathode was located at the axis. Here, we will also investigate the operation with a centrally-mounted cathode.

All analyses in this paper will be based on numerical simulations of a 5kW-class HET with a hollow cathode, conducted using the axisymmetric hybrid PIC/fluid code HYPHEN[20,30,31].

The rest of the paper is organized as follows. Sec. II presents the GPC model and its implementation within HYPHEN. Sec. III compares the simulation results obtained with both the GPC and LPC models for four plume sizes, with the cathode placed inside the MS. Sec. IV presents the results for both the GPC and LPC models and two plume sizes when the cathode is positioned outside the MS. Finally, Sec. V summarizes the conclusions.

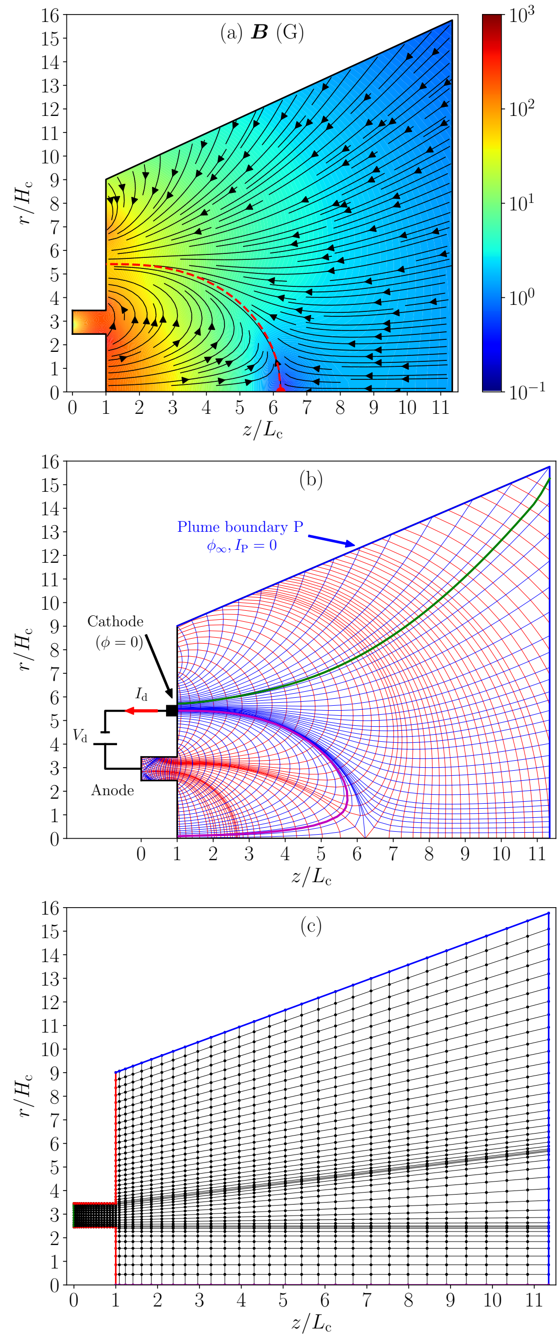

FIG. 1. (a) 2D (z,r) contour map and streamlines of $\boldsymbol{B}$. The dashed red line corresponds to the MS, and the red circle marker indicates the magnetic singular point. (b) The MFAM used by the E-module. Inner blue and red lines are B-parallel and B-perpendicular lines, respectively, defining the cells. The magenta and green lines correspond to the CML for cathodes 1 and 2, respectively. (c) The PIC mesh used by the I-module. The red, green and magenta lines indicate the thruster dielectric walls, the anode wall and the symmetry axis, respectively. All figures correspond to plume size P3.

II. SIMULATION DETAILS

A. Setup and model

A 5 kW-class HET similar to a PPS5000[32,33], with a conventional (non-shielded) magnetic topology and a hollow cathode is considered for this study. Figs. 1(b)-(c) sketch the simulation domain, which comprises the thruster annular vessel (with length $L_c = 29$ mm, width $H_c = 22.2$ mm and inner radius 54.5 mm), and a near-plume region of different sizes. Fig. 1(a) shows the applied magnetic field $\boldsymbol{B}$ magnitude map and streamlines. The peak of $B \equiv |\boldsymbol{B}|$ along the thruster channel midline is 196.05 G, at $z/L_c = 0.86$. The dashed red line in Fig. 1(a) indicates the (off-axis) MS in the near plume, which passes through the magnetic singular point located at the axis at $z/L_c = 6.2$. The magnetic lines are represented by the blue lines in Fig. 1(b). Downstream of the MS, the magnetic topology exhibits a magnetic nozzle (MN) shape, which will channel the plasma beam in the far plume[34].

The thruster anode covers the complete channel back wall and the cathode, located at the thruster exit plane, can be either externally-mounted (i.e., off-axis), as depicted in Fig. 1(b), or centrally-mounted (i.e., at the axis). A power source sets a discharge voltage $V_d = 300$ V between anode and cathode. The reference of the electric potential ϕ is set at the cathode, so that the potential of the anode wall is V_d. The thruster operates with xenon and the total neutral mass flow rate injected into the domain is $\dot{m} = \dot{m}_A + \dot{m}_C$, where $\dot{m}_A = 17.59$ mg/s and $\dot{m}_C = 1.32$ mg/s are the flow rates injected through the anode and the cathode, respectively (details on neutral injection conditions can be found in Ref. 20). The discharge current I_d collected at the anode wall provides the electron flow injected at the cathode. The temperature of the electrons emitted from the cathode is set to 2.25 eV.

The plasma discharge is simulated with the axisymmetric hybrid code HYPHEN, whose characteristics have been detailed in previous works[20,30,35,36] and are briefly outlined next. The code is composed of three main modules coupled within a time-marching sequential loop. The ion (I)-module operates on a structured mesh of the simulation domain, shown in Fig. 1(c), and implements a PIC method to solve the dynamics of the heavy species (i.e., ions and neutrals, including singly and doubly charged ions; charge exchange collisions (CEX) generating slow ions and fast neutrals in the plume are also considered) obtaining the net ion density n_i and ion current density vector $\boldsymbol{j}_i$.

The electron (E)-module solves a quasineutral drift-diffusion fluid model for the magnetized electron population on an unstructured magnetic field align mesh (MFAM)[37], obtained from $\boldsymbol{B}$ and shown in Fig. 1(b), where red lines correspond to magnetic equipotential lines. Setting the plasma density $n_e = n_i$, it provides the solution for the electric potential ϕ, the electron temperature T_e, the electron current density vector $\boldsymbol{j}_e$ (and thus the electric current density vector $\boldsymbol{j} = \boldsymbol{j}_e + \boldsymbol{j}_i$), and the energy flux vector $\boldsymbol{P}''_e = 5 n_e T_e \boldsymbol{u}_e/2 + \boldsymbol{q}_e$ (sum of enthalpy and heat fluxes). Full details on the electron fluid model equations can be found in Sec. III.A of Ref. 20 and Sec. 2.1 of Ref. 36; the numerical treatment of these equations is described in the Appendix B of Ref. 36. Interpolation between the PIC mesh and the MFAM is required to transfer plasma properties. The axisymmetric electron fluid model needs to be completed with empirical submodels for electron-wall interaction properties and for turbulent cross-field transport due to high-frequency plasma waves driven by kinetic and fluid instabilities.

As in Ref. 20, here we set a turbulent electron collisionality of the form $\alpha_t \omega_{ce}$, with $\omega_{ce} = eB/m_e$ the electron cyclotron frequency and α_t a "step-out" type tuning function representing the local electron turbulence level, which features two calibration parameters $\alpha_{t1} = 1.2\%$ and $\alpha_{t2} = 4.8\%$, fitted to reproduce PPS5000 the experimental values for I_d and thrust (F) at the operating point under consideration. The transition point from α_{t1} to α_{t2} is located downstream the B peak, at $z/L_c = 1.49$, and the corresponding value of α_t is kept constant along each magnetic line. Previous works have demonstrated the significance of accounting for the electron anomalous transport in the near plume on the cathode-beam coupling process[25]. In this study, the same α_t parameters are assumed for all cases.

Non-neutral effects are limited to (infinitely) thin Debye sheaths that develop around the thruster walls. The sheath (S)-module of HYPHEN solves these sheaths through the planar, unmagnetized, collisionless, kinetic model detailed in the Appendix of Ref. 20. The model is restricted to electron-repelling sheaths, includes secondary electron emission at dielectric walls, and retains non-Maxwellian features of the electron velocity distribution function (VDF), such as the replenishment fraction of the VDF tail corresponding to impacting electrons[38], which is set here to 30%. The model permits to obtain the local sheath potential fall from the quasineutral plasma to the wall at both the thruster dielectric walls and at the anode conducting wall at known potential V_d. This provides the appropriate boundary conditions for the wall-collected electron current density $j_{ne} = \mathbf{1}_n \cdot \boldsymbol{j}_e$ and energy flux $P''_{ne} = \mathbf{1}_n \cdot \boldsymbol{P}''_e$ at each (quasineutral) MFAM boundary face, with $\mathbf{1}_n$ being the *outward* unit normal vector. The implementation is described in Sec. III.A of Ref. 20 and it is omitted here for simplicity.

B. Simulation cases

Four different plume domains (P1 to P4) are considered, featuring plume axial extensions of 100, 200, 300 and 400 mm ($3.4L_c$, $6.9L_c$, $10.3L_c$ and $13.8L_c$). For all cases, the plume domain extends radially up to 200 mm at the thruster exit plane (see Fig. 1). The radial extension of the downstream end increases with the plume

Simulation parameter	Units	Value
PIC mesh number of cells	-	969, 1284, 1509, 1734
PIC mesh number of nodes	-	1049, 1371, 1601, 2831
PIC mesh smallest grid size	mm	1
MFAM number of cells	-	1948, 2397, 3506, 4081
MFAM number of faces	-	4025, 4933, 7186, 8353
MFAM average cells skewness	(10^{-2}) -	7.06, 6.45, 5.49, 5.31

TABLE I. Main mesh parameters (values separated by commas correspond to plume sizes P1 to P4).

length and is set to 250, 300, 350 and 400 mm for P1 to P4 cases, respectively, so that the PIC mesh adapts to the ion beam expansion in the plume to limit particle depletion. As an example, Figs. 1(b) and (c) show the MFAM and the PIC mesh for domain P3, respectively. The main characteristics of the simulation domain meshes for plume sizes P1 to P4 are listed in Tab. I.

Each heavy species population (i.e., singly and doubly charged ions and neutrals) is controlled during the simulation by maintaining a target number of 200 and 500 macroparticles per cell (with a $\pm 10\%$ of tolerance) for plume sizes P1 and P2–P4, respectively. The ion-moving timestep is set to 15 ns, ensuring that the fastest doubly charged ions require at least two timesteps to cross the smallest PIC mesh cell. A total time of 900 μs is simulated, enough to capture a sufficiently large number of breathing mode cycles. All the numerical results in this work are averaged over several of these breathing mode cycles. Simulations are performed on a modern workstation using 30 threads. The total computational time ranges from approximately 8 to 40 hours for plume sizes P1 to P4.

As outlined in Sec. I, three distinct cathode configurations are considered: cathode 1 (C1) and cathode 2 (C2) correspond to an externally-mounted cathode positioned inside and outside the MS at radial distances of 120 mm and 126.6 mm, respectively, while cathode 3 (C3) represents a centrally-mounted cathode aligned with the thruster axis. The magenta and green lines in Fig. 1(b) represent the corresponding closed and open CML for C1 and C2, with the latter intersecting the downstream axial boundary below the top right corner of the plume domain. For C3 the CML coincides with the symmetry axis. For plume size P1 and cathode C1, the axial downstream boundary of the plume intersects the closed CML and the magnetic singular point is left outside the plume domain.

C. Conditions at the plume boundary

Consider the case where the plasma beam from the HET expands into free space (or into a large vacuum chamber with low background pressure). The blue line in Fig. 1(b) represents the boundary P of the simulated plume. Boundary conditions must be defined at each point on P, ensuring they are "compatible" with the expected plasma behavior between P and infinity. It is assumed that the plasma beam is current-free, and that the electric potential decreases monotonically to a value ϕ_∞ at infinity (with respect to the cathode). This implies that: first, the current-free condition applies at P as well; and second, ions exiting the simulated plume domain will ultimately reach infinity, while individual electrons leaving P may either reach infinity or be reflected back into the simulation domain. The electron fluid model, as used in HYPHEN, must be consistent with this behavior.

As discussed in Sec. I, the conventional approach is to apply a local plume condition (LPC), which replaces the global zero-current condition with the more restrictive, yet simpler to implement, condition of zero local current, that is

$$j_{\mathrm{neP}} = -j_{\mathrm{niP}}, \tag{1}$$

at any point of the boundary P. In addition, the electron energy flux is set to

$$P''_{\mathrm{neP}} = -cT_{\mathrm{eP}}j_{\mathrm{neP}}/e, \tag{2}$$

where the positive constant c is set empirically.

Previous HYPHEN simulations for a magnetically shielded HET reported in Ref. 20 used $c = 9/2$. Other studies have set T_{eP}, instead of P''_{neP}, in both multi-fluid[22,26] and hybrid[17,27] HET simulations. The 2D hybrid HET simulations in Ref. 39 applied a Neumann boundary condition, $dT_{\mathrm{e}}/d\mathbf{1}_{\mathrm{n}} = 0$ at P, which is equivalent to $q_{\mathrm{neP}} = 0$, thus yielding $c = 5/2$. Multi-fluid simulations of a magnetic nozzle have shown that electron cooling is highly sensitive to the type of boundary condition (i.e., Dirichlet or Neumann) applied to T_{eP}[40]. HYPHEN simulations of an electrodeless plasma thruster in Ref. 36 used $c = 5/2$, $9/2$ and $13/2$, revealing a significant impact of c on the electron temperature, with $c = 9/2$ providing the best agreement for two plume domain sizes. Here, we set $c = 9/2$ when the LPC is applied.

As an alternative to the LPC, we propose here a global plume condition (GPC) which imposes the global zero current condition at P as

$$I_{\mathrm{P}} = I_{\mathrm{eP}} + I_{\mathrm{iP}} = \int_{\mathrm{P}} [j_{\mathrm{ne}}(\phi_{\infty\mathrm{P}}) + j_{\mathrm{ni}}] dS = 0, \tag{3}$$

where: the surface integral is performed over P; I_{eP} and I_{iP} are the outwards electron and ion currents at P, respectively; j_{niP} is provided by the I-module at any point of P; and, assuming a Maxwellian VDF for electrons, $j_{\mathrm{neP}}(\phi_{\infty\mathrm{P}})$ is

$$j_{\mathrm{neP}}(\phi_{\infty\mathrm{P}}) = -en_{\mathrm{eP}}\sqrt{\frac{T_{\mathrm{eP}}}{2\pi m_{\mathrm{e}}}} \exp\left(\frac{-e\phi_{\infty\mathrm{P}}}{T_{\mathrm{eP}}}\right), \tag{4}$$

at any point of P, with $\phi_{\infty\mathrm{P}} = \phi_{\mathrm{P}} - \phi_\infty \geq 0$, being ϕ_{P} the electric potential at the (quasineutral) plume boundary P. Eq. (3) is an implicit equation for ϕ_∞, which is solved iteratively [by linearizing Eq. (4)]. Thus, the resulting value of ϕ_∞ satisfies $I_\mathrm{P} = 0$. Once ϕ_∞ is known, the boundary condition j_neP at any point of P is known from Eq. (4).

With respect to the electron energy flux, we assume at infinity the expression

$$P''_{\mathrm{ne}\infty} = -2T_\mathrm{eP} j_\mathrm{neP}/e, \tag{5}$$

based again on a Maxwellian electron VDF. Then the boundary condition at P for the energy flux is

$$P''_\mathrm{neP} = P''_{\mathrm{ne}\infty} - j_\mathrm{neP}\phi_{\infty P} = -j_\mathrm{neP}\frac{T_\mathrm{eP}}{e}\left(2 + \frac{e\phi_{\infty P}}{T_{eP}}\right). \tag{6}$$

Notice that the sum between parentheses would correspond here to the arbitrary constant c in Eq. (2).

III. INFLUENCE OF PLUME SIZE AND BOUNDARY CONDITIONS

Solutions for plume sizes P1 to P4 with C1, and using the GPC and LPC, are compared here. The eight simulation cases will be denoted as GPiC1 and LPiC1 ($i = 1, 2, 3, 4$), corresponding to the GPC and LPC, respectively. We begin with the maps of electric and electron currents, as these are the most significantly affected. This is followed by the maps of scalar plasma variables, and finally, the performance results.

Fig. 2 plots the in-plane electric current density $\tilde{\boldsymbol{j}} = \boldsymbol{j} - j_\theta \mathbf{1}_\theta$ for plume sizes P1 to P3 (P4 results are similar for GPC and LPC and thus omitted). All of them satisfy $I_\mathrm{P} = 0$, [i.e. $I_\mathrm{iP} = |I_\mathrm{eP}|$ in all cases, according to Eq. (3)]. The boundary condition at P affects mainly the $\tilde{\boldsymbol{j}}$ solution downstream of the CML. In this region, the LPC forces all current loops to close within the plume domain. Therefore, current loops outward of the CML are clearly different for different plume sizes. In contrast, with the GPC, current loops change less with the plume size since they are not constrained to close within the plume domain (the electric current at P can be locally nonzero), which makes GPC more robust against plume truncation and more physically plausible. The LPC provides a good approximation only when the simulated plume domain is sufficiently large. In both LP4C1 and GP4C1 cases, the null electric current point ($\tilde{\boldsymbol{j}} = \mathbf{0}$) in the bulk plume downstream the CML is located at $(z/L_\mathrm{c}, r/H_\mathrm{c}) \approx (7.6, 4.6)$. A more pronounced variation in the location of this point with plume size is observed in LPC cases compared to GPC cases. In particular, for LP2C1 it is located at $(z/L_\mathrm{c}, r/H_\mathrm{c}) \approx (4.9, 7.3)$, corresponding to axial and radial shifts of approximately 36% and 59%, respectively, relative to P4. In contrast, for GP2C1 the point is found at $(z/L_\mathrm{c}, r/H_\mathrm{c}) \approx (6.4, 6.3)$, corresponding to smaller axial and radial shifts of about 16% and 37%, respectively.

Focusing now on the region inwards the CML, similar anode-to-cathode current loops are found for cases P2 to P4, but not for P1, where part of the CML has been left outside the plume. This indicates that P1 is not a good choice for the simulations: when the cathode is placed inside the MS, the domain must include integrally the closed CML. Nonetheless, the case GP1C1 outperforms LP1C1 since its $\tilde{\boldsymbol{j}}$ solution remains closer to that of the P2-P4 cases.

For the eight simulation cases the solution for the in-plane ion current density, $\tilde{\boldsymbol{j}}_\mathrm{i} = \boldsymbol{j}_\mathrm{i} - j_{\theta\mathrm{i}}\mathbf{1}_\theta$, is practically identical, and exhibits the characteristic ion divergence of a HET plume; it is shown in Fig. 3(a) for size P3. The ion beam current through P, I_iP, is practically the same for all cases and approximately equal to 16.66 A, with maximum differences of about 2%. The ion population downstream of the CML is dominated by fast ions generated from ionization inside the thruster channel, whereas slow ions produced in the plume through CEX constitute a minor fraction contributing less than 1% of I_iP. Variations in the electric potential among cases downstream of the CML (shown later) are much smaller than V_d (or the average ion energy in that region), so that the main ion flow is practically unaffected. The main differences among GPC and LPC cases are found in the dynamics of the slow CEX ions in the lateral part of the plume, as discussed later. Note that downstream of the MS, where the magnetic topology features a MN shape, the near-unmagnetized ions detach inwardly from the magnetic lines, as expected[41].

Differences on $\tilde{\boldsymbol{j}}$ among cases are thus due quasi exclusively to $\tilde{\boldsymbol{j}}_\mathrm{e}$. Figs. 3(b) and 3(c) show this current for cases GP3C1 and LP3C1, respectively. For the two cases, the center of the electron beam travels along the CML. The component of this beam closest to the MS diffuses towards it and then exits outwards, primarily near the magnetic singular point, to neutralize the ion beam. The main difference between the LPC and the GPC is found in the electron flow towards the lateral plume boundary. The LPC promotes electron detachment from the magnetic lines, yielding a higher electron current towards the lateral plume boundary to locally cancel the ion current there (mainly carried by high-divergence fast ions and slow CEX ions). In contrast, the GPC reduces the electron current towards the lateral plume boundary, and the resulting electron streamlines follow more closely the local magnetic field lines, exhibiting a more progressive outward detachment towards the lateral boundary. This solution is more representative of the still well-magnetized electron population in the simulated plume region: the surface-averaged values over P of B and the effective Hall parameter, for plume sizes P1 to P4, decrease from 7.4 to 1.8 G, and from 212.2 to 68.1, respectively.

Even though the electron current density at the lateral plume boundary is relatively low, on the order of 10^{-5} to 10^{-3} Acm^{-2}, the difference in lateral electron flow between the LPC and the GPC is physically relevant: in case GP3C1, approximately 10% of $|I_\mathrm{eP}|\,(= I_\mathrm{iP})$ is collected at the lateral plume boundary, whereas this

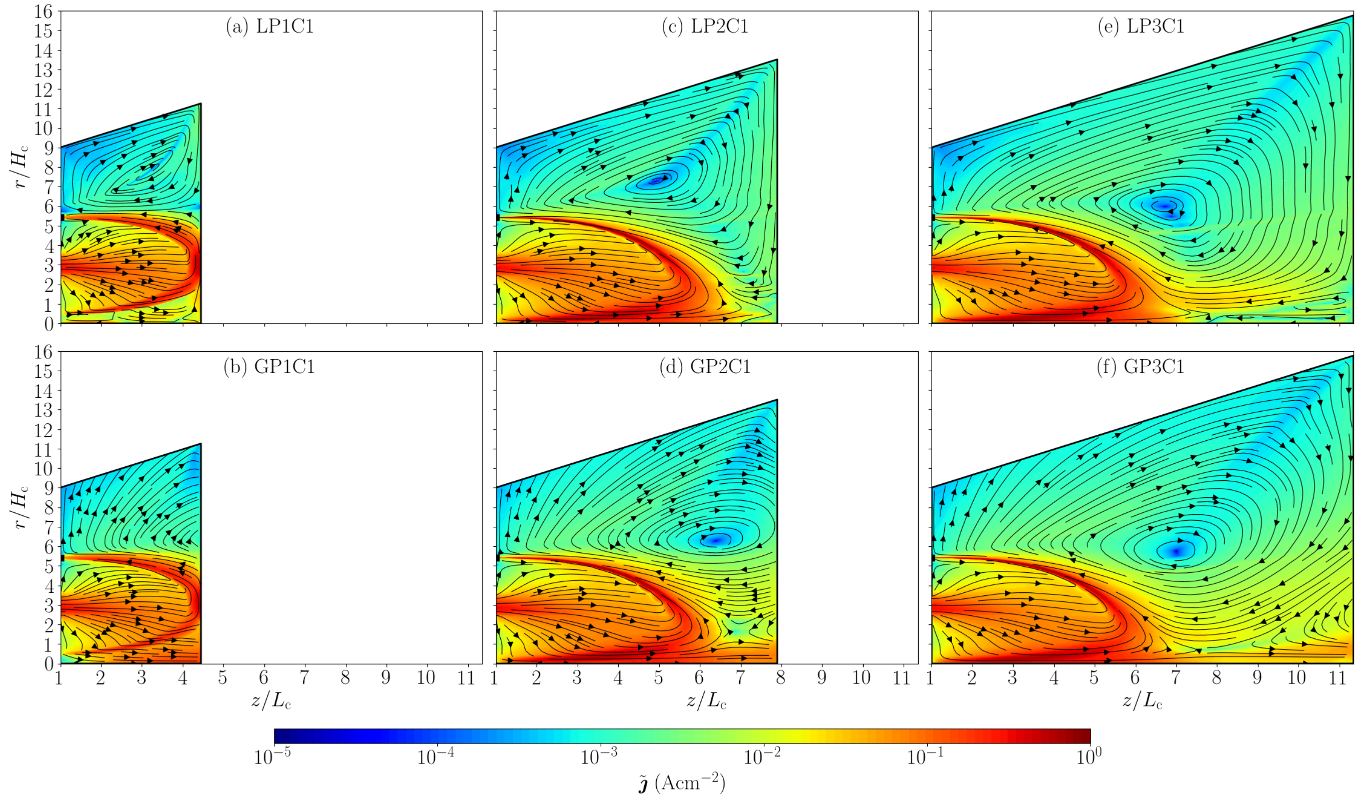

FIG. 2. Plume sizes P1-P3 with C1 (black square marker) and with LPC (top row) and GPC (bottom row). 2D (z,r) contour maps and streamlines of $\tilde{\boldsymbol{j}}$.

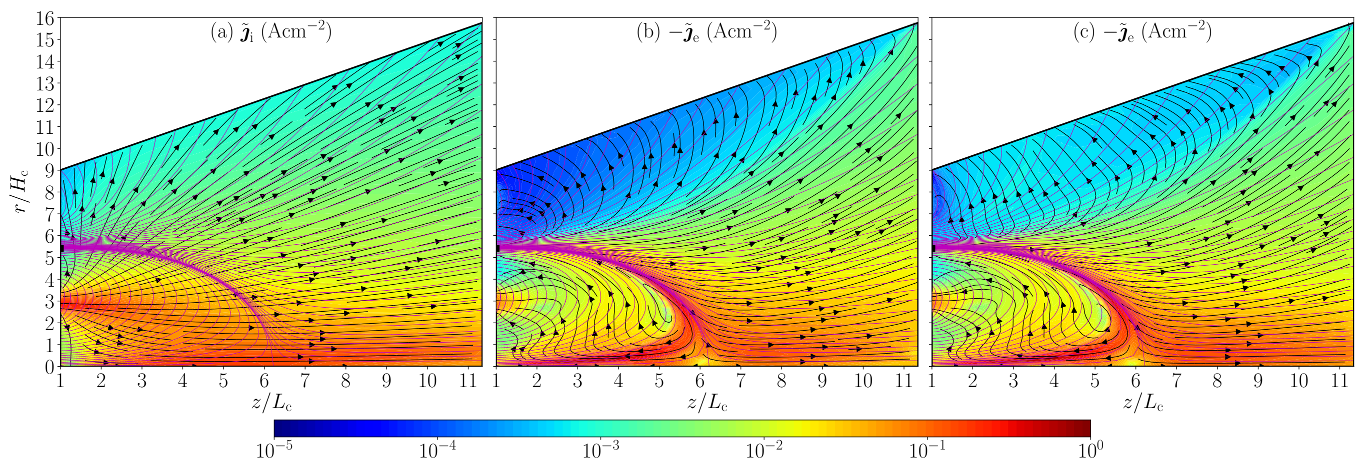

FIG. 3. 2D (z,r) contour maps of (a) $\tilde{\boldsymbol{j}}_i$ and (b) $\tilde{\boldsymbol{j}}_e$ for case GP3C1, and (c) $\tilde{\boldsymbol{j}}_e$ for case LP3C1. The black lines with arrows depict streamlines of $\tilde{\boldsymbol{j}}_i$ in (a) and $-\tilde{\boldsymbol{j}}_e$ in (b) and (c). Magenta lines indicate magnetic lines. The black square marker indicates the location of cathode 1.

fraction increases to 14% in case LP3C1. This result is in line with the simulations using the LPC reported in Ref. 25, where the authors note that if the plume boundaries are set too close to the channel exit, the transport of electrons in the near plume gets perturbed by the zero local current condition, and more electron current across magnetic field lines may occur. Electron detachment near the plume boundary has also been observed in HYPHEN simulations of an electrodeless plasma thruster with a MN, where the LPC was used[36].

Fig. 4 compares relevant plasma variables at the plume boundary P for all cases with plume size P3. The spatial variable runs first along the axial boundary, from the axis to the upper-right corner, and then continues from

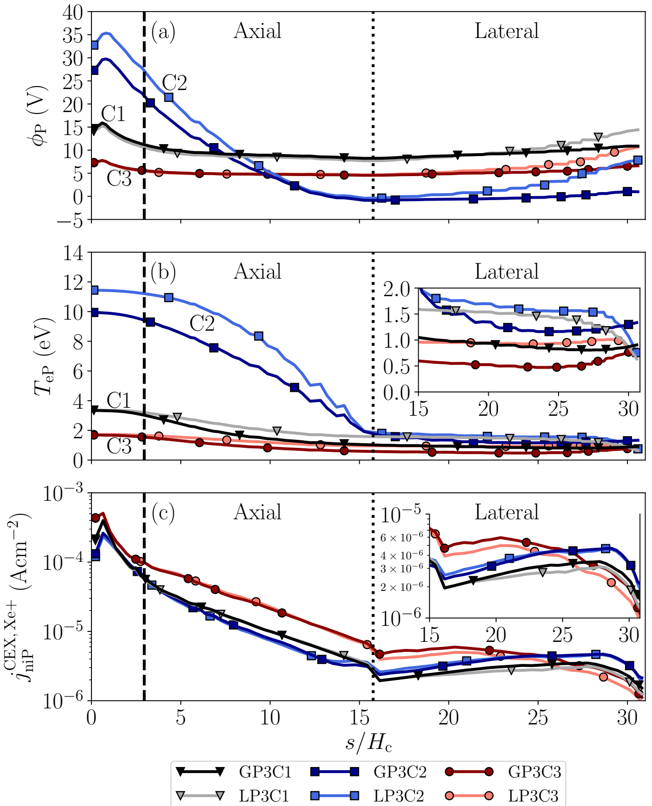

FIG. 4. Plume size P3. Comparison of profiles along P for the GPC and LPC. (a) $\phi_{\rm P}$, (b) $T_{\rm eP}$ and (c) the current density of singly charged slow CEX ions $j_{\rm niP}^{\rm CEX,Xe+}$. Coordinate s runs along P with $s = 0$ at the symmetry axis. The vertical black dashed and dotted lines correspond to the thruster channel midradius and the upper-right corner of the plume domain, respectively.

there up to $z/L_{\rm c} = 1$, along the lateral boundary [refer to Fig. 1(b)]. We focus now on the results for C1 cases. Figs. 4(a) and 4(b) show the electric potential and the electron temperature profiles, respectively. Compared to case GP3C1, the larger electron current at the lateral plume boundary in case LP3C1 leads to an increase in $\phi_{\rm P}$ of up to approximately 30% in that region. These differences in $\phi_{\rm P}$ between cases are on the order of the local electron temperature, and are therefore significant for near-plume diagnostics. The electron temperature also exhibits non-negligible differences between the two cases, with lower values for case GP3C1 along most of the plume boundary. In particular, at the lateral boundary, $T_{\rm eP}$ in LP3C1 is up to about 70% higher than in GP3C1. An added value of the GPC is that the average energy deposited at P by exiting electron, $\mathcal{E}_{\rm neP} - eP''_{\rm neP}/j_{\rm neP}$, is computed from Eq. (6) yielding values ranging from $4.0T_{\rm eP}$ to $9.2T_{\rm eP}$ for case GP3C1, whereas the LPC sets it "arbitrarily" to $4.5T_{\rm eP}$. According to Eq. (6), this implies that $e\phi_{\infty\rm P}/T_{\rm eP} \approx 2.0$-$7.2$ for case GP3C1.

Fig. 4(c) compares the current density profiles at P of singly charged CEX ions, $j_{\rm niP}^{\rm CEX,Xe+}$. The differences in $\phi_{\rm P}$ at the lateral plume boundary between GP3C1 and LP3C1 cases affect the dynamics of CEX ions. In particular, the higher $\phi_{\rm P}$ in case LP3C1 reduces $j_{\rm niP}^{\rm CEX,Xe+}$ by up to 16%, while increasing the average energy of these ions at P (not shown) by up to 11%. Although, as previously discussed, CEX ions constitute a minor population in the plume (contributing only about 1% to the fraction of $I_{\rm iP}$ through the lateral plume boundary) their accurate characterization is essential for assessing plume–satellite interaction effects.

Fig. 5 shows the axial profiles of ϕ and $T_{\rm e}$ along the channel midline for $z/L_{\rm c} \geq 3$. The plasma density $n_{\rm e}$ is very similar for all cases and it is omitted for simplicity. For $z/L_{\rm c} < 3$ (not shown), all cases present very similar profiles for all variables, with peak values $T_{\rm e} \approx 28$ eV and $n_{\rm e} \approx 1.7 \cdot 10^{18}$ m^{-3}. We focus now on the profiles for C1 cases. Despite the significant changes across different cases on plasma variables in the lateral part of the plume commented above (especially in the plasma current maps), there is consistency on these profiles for the different plume sizes and boundary conditions.

ALTERNATIVA AL TEXTO ANTERIOR: Focusing now on C1 cases (C2 and C3 cases will be analyzed in Sec. IV), the results show only moderate relative variations on ϕ and $T_{\rm e}$ along the channel midline across cases (especially for sizes P2-P4), despite the significant differences observed in the plasma current maps and in ϕ and $T_{\rm e}$ at the lateral plume boundary, as discussed above.

Tab. II lists the main performance figures for the eight simulation cases, beginning with the cathode coupling voltage, $V_{\rm cc}$. For plume size P1, $V_{\rm cc}$ values correspond to the electric potential at the plume boundary at the channel midradius. For plume sizes P2-P4, $V_{\rm cc}$ is estimated as the electric potential value at the crossing point between the channel midline and the CML[42]. For both the LPC and GPC, the largest differences in $V_{\rm cc}$ are found for plume size P4. These discrepancies result from minor variations on the CML due to the nontrivial optimization of the MFAM cell layout for large plume domains, and do not reflect any significant physical change in the cathode-beam coupling process. Mesh-induced variations in $V_{\rm cc}$ have been quantified to be approximately ± 3 V. Nonetheless, the largest differences in $V_{\rm cc}$ across P2-P4 cases are on the order of 1% of $V_{\rm d}$. This indicates a very similar effective ion acceleration in the discharge for all cases, which is in line with the very small differences (below 2%) observed in the thrust, F, among cases, as listed in Tab. II. The values of $F_{\rm e}$ and $F_{\rm i}$ correspond to the contributions to thrust (i.e., the downstream axial momentum fluxes) from the electron and ion species, including CEX populations. The contribution to thrust from neutral species remains approximately 1 mN across all cases. As expected, electron momentum flux is transferred to ion momentum flux as the plasma beam moves downstream. The small increase (on average) in thrust with the plume size is due to the small magnetic force over the plasma there. It is assumed that the residual magnetic force between P and infinity has no relevant

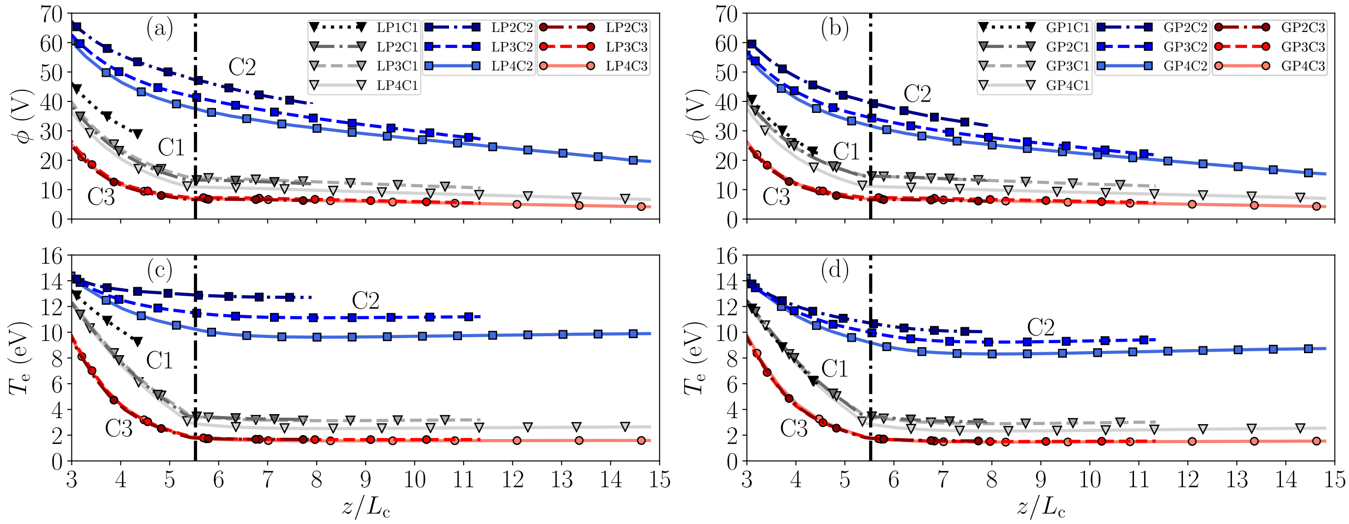

FIG. 5. 1D axial profiles along the thruster channel midline in the near-plume region for cases with the LPC (left column) and the GPC (right column). The vertical black dot-dashed line indicates the crossing point with the MS at $z/L_c = 5.5$.

	GP1C1	GP2C1	GP3C1	GP4C1	LP1C1	LP2C1	LP3C1	LP4C1
V_{cc} (V)	21.39	14.52	14.90	11.39	26.00	13.21	13.98	11.07
ϕ_∞ (V)	5.80	6.17	4.31	1.33	N/A	N/A	N/A	N/A
F (mN)	280.1	284.0	283.9	286.5	279.6	286.0	284.8	286.1
F_i (mN)	274.7	280.6	281.1	284.4	272.3	282.3	281.9	284.0
F_e (mN)	4.3	2.4	1.7	1.0	6.3	2.8	1.9	1.0
η	0.39	0.40	0.40	0.41	0.39	0.40	0.40	0.41
η_{ene}	0.65	0.64	0.65	0.65	0.65	0.64	0.64	0.65
η_{div}	0.77	0.78	0.79	0.77	0.77	0.78	0.78	0.78
η_{disp}	0.78	0.80	0.78	0.81	0.78	0.80	0.80	0.80

TABLE II. Performance figures for plume sizes P1 to P4 with C1 and the GPC and LPC.

impact in thrust.

An important asset of the GPC is the determination of the potential at infinity, ϕ_∞, also given in Tab. II for the four plume sizes. For sufficiently large plumes, i.e., plume sizes P2-P4, ϕ_∞ monotonically decreases with the plume size. The total decrease from P2 to P4 amounts to about 78% of its value for P2: 30% from P2 to P3 and 48% from P3 to P4. This suggests that simulating a plume size larger than P4 would be necessary for a more precise estimation of ϕ_∞. However, the results indicate that increasing the plume size leads to only incremental variations in ϕ along the thruster channel midline and F, and thus the effect on discharge performance is minimal. Moreover, the quality of the MFAM tends to deteriorate significantly for very large plumes. For plume size P4, mesh-induced variations in ϕ_∞ are lower than those stated before for V_{cc}, and amount just to ± 1 V, approximately.

The plasma power balance is detailed in the Appendix A and shows only small variations (below 2%) in its different contributions across cases. The discharge current, I_d, is practically the same for all cases, and approximately equal to 17.84 A, with maximum differences of about 1%. Therefore, for all cases the total power deposited into the plasma is $P \simeq V_d I_d \approx 5.4$ kW, and the thrust efficiency is $\eta = F^2/(2\dot{m}P) \approx 40\%$. According to Eq. (A.2), η is conveniently factored as the product of three partial efficiencies, which are defined in Eq. (A.3): the energy efficiency, η_{ene}, which represents the fraction of the total power deposited into P; the divergence efficiency, η_{div}; and the dispersion efficiency, η_{disp}. The latter two partial efficiencies are plume-related metrics that assess plume divergence and velocity dispersion, respectively. These partial efficiencies also show slight changes (maximum 3%) between cases. (Note that we aim to highlight here that the differences between cases are minimal and not the values themselves.)

Therefore, for a cathode located inside or at the MS, and provided that the size of the simulated plume region is sufficiently large such that ϕ variations in the downstream part of the plume are much smaller than V_d, we conclude that thruster performance is well determined regardless of whether the LPC or GPC is used. Nonetheless, it is evident that plume size and conditions significantly impact plasma current maps within the plume and the solution for ϕ and T_e in the lateral part of the plume which is important for plume characterization and comparison with experimental data (noting that the plume is the plasma region most accessible to diagnostics).

Finally, Figs. 5(c) and 5(d) reveal that for sizes P2-P4, T_e remains nearly constant at relatively low values, around 2.5 eV, downstream the MS, and no significant electron cooling is observed, in line with the results in Ref. 26. Previous kinetic studies on magnetized plumes have shown that the total potential fall to infinity in the plume is primarily determined by the electron thermal energy[43]. Here, the surface-averaged value of $e\phi_{\infty P}/T_{eP}$ over P varies slightly with plume size, ranging between

4.7 and 5.7 (which, taking $T_{\mathrm{iP}}/T_{\mathrm{eP}} \approx 10$, as obtained here, agrees very well with simulations for a magnetic nozzle in Ref. 43). Since $T_{\mathrm{eP}} \sim 1\mathrm{eV}$, $\phi_{\infty\mathrm{P}}$ still amounts to about 15-20% of the potential drop in the near plume downstream of $z/L_{\mathrm{c}} = 3$. Increasing plume size results in only a small decrease in ϕ_{P} and the Hall parameter, but not in T_{eP}. This suggests that anomalous parallel-field electron cooling[44] should be considered in the MN region of the plume, similar to the approach taken for electrodeless plasma thruster simulations with HYPHEN in Ref. 36.

IV. EFFECTS OF CATHODE LOCATION ON CURRENT MAPS AND CATHODE COUPLING

This section presents an analysis of the results for plume sizes P2 to P4 with C2 (i.e., an externally-mounted cathode positioned outside the MS) and C3 (i.e., a centrally-mounted cathode aligned with the thruster axis), considering both the GPC and LPC. The corresponding simulation cases will be referred to as GPiCj and LPiCj ($i = 2, 3, 4$; $j = 2, 3$) for the GPC and LPC, respectively. We begin by analyzing the maps of electric and electron currents, as these are the most strongly affected by the cathode location, and clearly demonstrate that the LPC produces unreliable results for C2 cases. Therefore, the remainder of the discussion focuses on the GPC cases, emphasizing the impact of cathode location on the solutions for ϕ, T_{e}, and n_{e} in the plume, as well as on the main performance figures. The trends found on these plasma parameters show good agreement with previous numerical and experimental studies.

Figs. 6(a)-(d) show $\tilde{\boldsymbol{j}}$ for C2 cases with plume sizes P3 and P4. As discussed in Secs. II B and III, for plume sizes P2-P4 and C1, the CML is enclosed by the MS (blue dashed line in Fig. 6), forming a closed loop within the simulated plume domain, which is located sufficiently far from the P boundary. In contrast, for C2 cases, the CML (red dashed line in Fig. 6) extends downstream along the plume and intersects the P boundary. The anode-to-cathode current loop closes downstream of the MS, below the CML, and a second counter-rotating current loop forms above the CML. When the LPC is applied, current streamlines of these two counter-rotating current loops are constrained to be parallel to the P boundary, so that they must necessarily converge at a plasma stagnation point at P featuring $\tilde{\boldsymbol{j}} = 0$. Therefore, the current solution provided by the LPC is inherently dependent on the plume size: observe in Figs. 6(a) and (c) how, for cases LP3C2 and LP4C2, this point moves with the downstream boundary of the plume, and the electric current loops in the near plume exhibit notable differences in the region common to both cases. On the other hand, by locally decoupling ion and electron currents at P, the GPC allows these current loops to close *at infinity*. As a result, the influence of the P boundary on the current solution is significantly reduced, making it more robust to variations in plume size. In particular, the plasma stagnation point at P, which is induced artificially by the LPC, is absent when the GPC is applied. Instead, a $\tilde{\boldsymbol{j}} = 0$ point appears within the domain, located at a similar position for both P3 and P4 sizes.

Figs. 6(e) and 6(f) show $\tilde{\boldsymbol{j}}_{\mathrm{e}}$ for cases LP3C2 and GP3C2, respectively. The central part of the electron beam emitted by cathode C2 travels downstream along the CML and yields a local maximum in the $\tilde{\boldsymbol{j}}_{\mathrm{e}}$ magnitude near the upper-right corner of the plume domain, where the CML intersects the P boundary. Note the magnetic separation of these electrons, similar to that of C1 cases. Now, only the fraction of electrons emitted by the cathode closest to the MS travels along it towards the singular point, where they penetrate into the interior region of the separatrix and subsequently into the thruster channel. This behavior has also been observed in three-dimensional hybrid simulations of the near plume of a HET with a similar magnetic topology, when the external cathode is placed in the lateral region of the plume, outside the MS[21].

Fig. 7 shows $\tilde{\boldsymbol{j}}$ and $\tilde{\boldsymbol{j}}_{\mathrm{e}}$ maps for C3 cases with plume size P3 (as in C1 cases, results for size P4 are similar with both the GPC and LPC and are therefore omitted for simplicity). The solutions for $\tilde{\boldsymbol{j}}$ and $\tilde{\boldsymbol{j}}_{\mathrm{e}}$ downstream of the MS closely resemble those found for C1 cases, as described in Sec. III. The main differences compared to C1 cases arise in the anode-to-cathode current loop inside the MS: the centrally-mounted cathode generates significantly higher local $\tilde{\boldsymbol{j}}$ and $\tilde{\boldsymbol{j}}_{\mathrm{e}}$ in the cathode near-plume along the axis and enhances the coupling between cathode electrons and the ion beam exiting the thruster channel (see later). This improvement occurs because the outermost component of the electron beam emitted from the cathode diffuses towards the thruster exit plane well upstream of the MS, prior to reaching it.

As in C1 cases, plume size and boundary condition have minimal impact on $\tilde{\boldsymbol{j}}_{\mathrm{i}}$ for C2 and C3 cases (maps are omitted for brevity). The main effect of cathode location appears in the ion divergence, as discussed later. Therefore, the differences in $\tilde{\boldsymbol{j}}$ stem primarily from variations in $\tilde{\boldsymbol{j}}_{\mathrm{e}}$ induced by the plume condition, following the same trend as in C1 cases: compared to the GPC, the LPC promotes electron detachment from magnetic lines, leading to a higher electron current towards the lateral plume boundary [compare Figs. 6(e) and 6(f) for C2, and Figs. 7(c) and 7(d) for C3]. As discussed in Sec. III for C1 cases, this yields higher ϕ_{P} (and T_{eP}) values at the lateral plume boundary [refer to Figs. 4(a) and 4(b)]. The differences between the LPC and GPC are larger (smaller) in C2 (C3) cases, respectively, and relevant for plume diagnostics in all cases. Additionally, there is a comparable influence on the current density of CEX ions at the lateral part of the plume boundary (see Fig. 4(c)]. Given the strong impact of plume size on the current solution in C2 cases when the LPC is applied, the following analysis focuses exclusively on GPC cases.

We next examine the main performance figures for C2

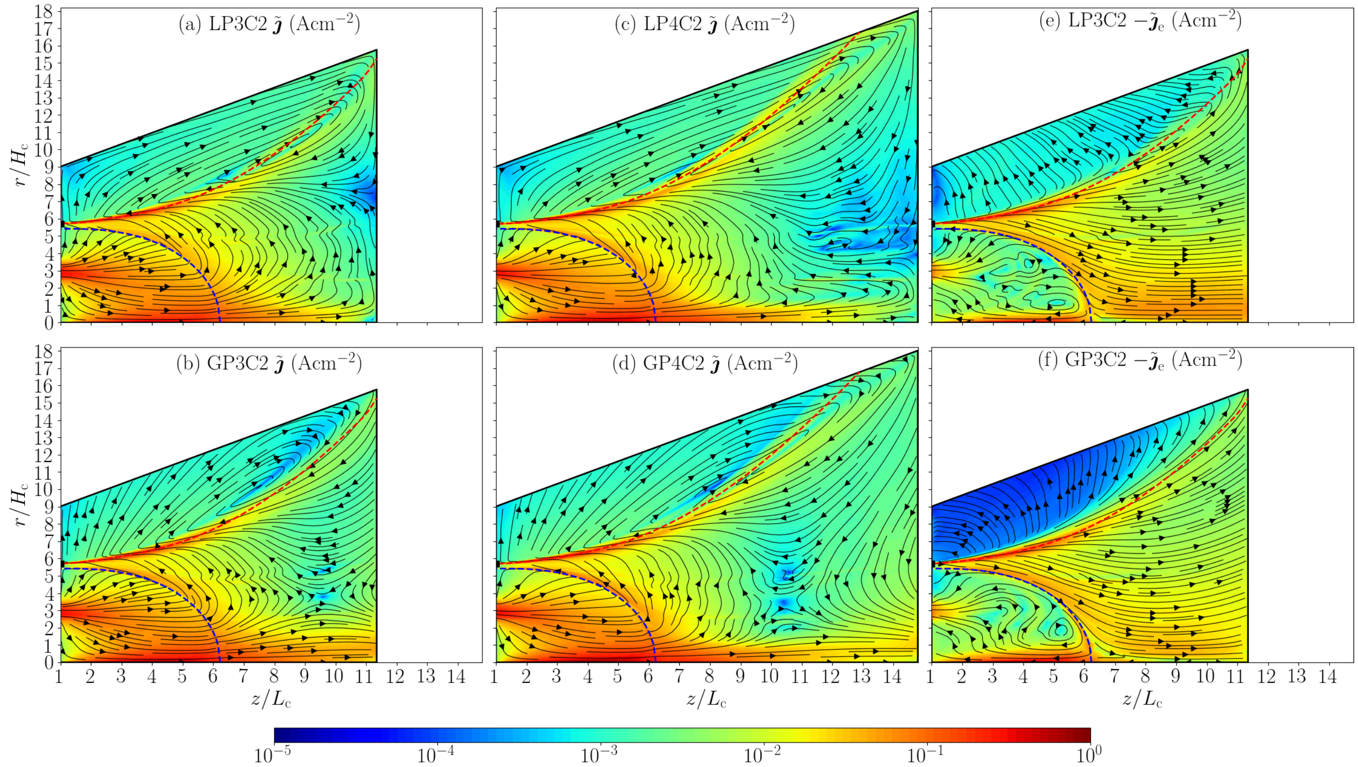

FIG. 6. Results with C2 (black square marker) and with LPC (top row) and GPC (bottom row). 2D (z,r) contour maps of $\tilde{\boldsymbol{j}}$ for plume sizes P3 and P4 (a)-(d), and $\tilde{\boldsymbol{j}}_e$ for plume size P3 (e)-(f). The black lines with arrows depict streamlines of $\tilde{\boldsymbol{j}}$ and $-\tilde{\boldsymbol{j}}_e$. The red and blue dashed lines correspond to the CML and the MS, respectively.

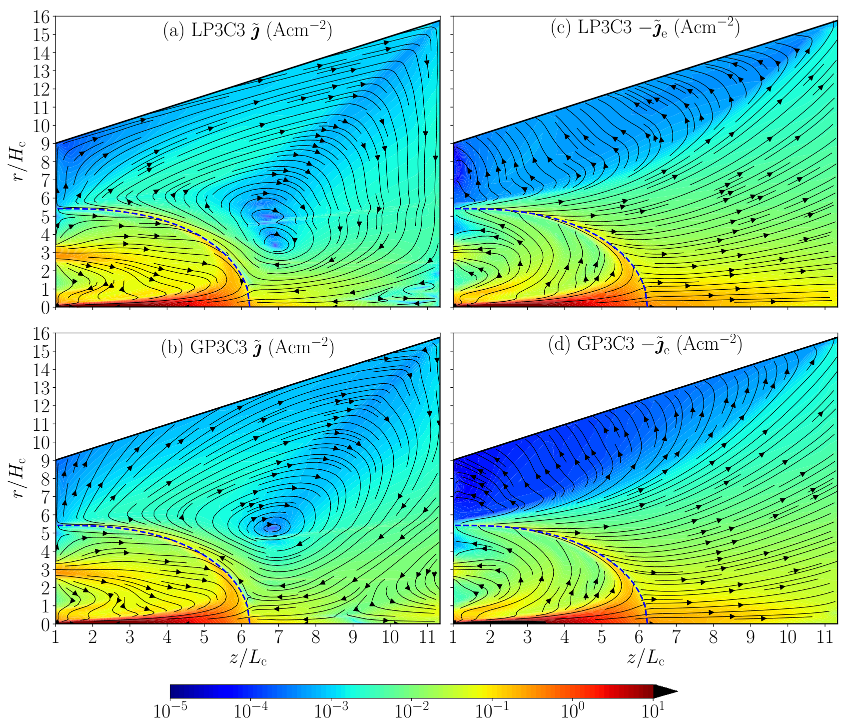

FIG. 7. Plume size P3 with C3 (black square marker) and with LPC (top row) and GPC (bottom row). 2D (z,r) contour maps of $\tilde{\boldsymbol{j}}$ (a)-(b) and $\tilde{\boldsymbol{j}}_e$ (c)-(d). The black lines with arrows depict streamlines of $\tilde{\boldsymbol{j}}$ and $-\tilde{\boldsymbol{j}}_e$. The blue dashed lines correspond to the MS.

	GP2C2	GP3C2	GP4C2	GP2C3	GP3C3	GP4C3
V_{cc} (V)	38.86	34.19	31.56	6.40	7.00	6.50
ϕ_∞ (V)	-4.95	-12.75	-14.78	2.65	2.10	0.74
F (mN)	271.4	272.1	275.2	297.1	294.9	296.6
F_{i} (mN)	264.5	267.1	271.7	294.1	292.3	294.3
F_{e} (mN)	6.0	4.1	2.6	1.6	1.1	0.7
η	0.37	0.37	0.38	0.42	0.42	0.42
η_{ene}	0.70	0.69	0.71	0.64	0.64	0.64
η_{div}	0.71	0.70	0.71	0.80	0.80	0.79
η_{disp}	0.75	0.76	0.76	0.82	0.82	0.84

TABLE III. Performance figures for plume sizes P2 to P4 for C2 and C3 cases with GPC.

and C3 cases, summarized in Tab. III. For both C2 and C3 cases, V_{cc} is estimated as the electric potential at the crossing point between the channel midline and the MS. This choice enables a more consistent comparison with C1 cases, and it is also physically motivated. In C3 cases, the CML is the symmetry axis, and a large fraction of cathode-emitted electrons is guided near the MS towards the channel midline [see Fig. 7(d)]. In C2 cases, the component of the cathode-emitted electron flow that enters the thruster channel travels along the MS toward the magnetic singular point [refer to Fig. 6(f)]. Therefore, the MS serves as a meaningful reference magnetic surface for characterizing the coupling between cathode electrons and the ion beam.

We focus first on the effects of cathode location for any plume size (P2 to P4). Reducing the cathode radial position (i.e., moving from C2 to C1 to C3) results in lower V_{cc}, and thus improved cathode-beam coupling, and higher values of both F and η (up to 5% in absolute terms). Since I_{d} also increases (from 17.26 to 17.84 to 18.22 A, respectively), and thus $P \simeq V_{\mathrm{d}} I_{\mathrm{d}}$, the higher η is attributed to the higher F. Furthermore, partial efficiencies reveal an increase in η_{div} (up to 10%) and η_{disp} (up to 8%), indicating lower plume divergence and velocity dispersion, and a decrease in η_{ene} (up to 7%).

Several experimental and numerical studies have reported results consistent with the behavior of V_{cc}, F, η, and plume divergence observed here. For an externally-mounted cathode, Ref. 1 reported a decrease in thrust with increasing radial position of the cathode, leading to the conclusion that the optimal cathode position is as close as possible to the outer magnet pole. Various experimental works have reported an increase in V_{cc} and poorer performance when increasing the radial position of the externally-mounted cathode, in particular for locations outside the MS[7–10]. Measurements on a HET with an externally-mounted cathode and a magnetic topology lacking an off-axis separatrix indicated that V_{cc} increased in magnitude with the radial position of the cathode when the cathode was moved across regions of high electron magnetization, where the effective Hall parameter was about 500[12]. Here, V_{cc} increases with the radial position of the cathode, i.e., moving from C3 to C1 to C2, being the corresponding effective Hall parameter in the cathode region about 52, 215 and 350, respectively. For a 6 kW HET, Jameson *et al.*[2] compared the performance with externally and centrally-mounted (i.e., on-axis) cathodes. Higher V_{cc} values were observed when operating with the externally-mounted cathode, while efficiency was reported to increase by 2-3% when using the centrally-mounted cathode. Compared to the operation with an externally-mounted cathode, reduced V_{cc} and plume divergence were also reported in Ref. 4 for a 8 kW HET with a centrally-mounted cathode. Full PIC 2D axial-radial simulations[28,29] have captured the lower plume divergence found in experiments when operating with a centrally-mounted cathode.

On the other hand, the higher the radial position of the cathode, the more pronounced the variations in all performance figures with plume size. The value of ϕ_∞ decreases with increasing plume size for all cathode positions, with C2 (C3) cases exhibiting the largest (smallest) variations, respectively. This behavior suggests that simulating sufficiently large plume domains is particularly important when the cathode is located outside the MS.

We focus now on the solutions for ϕ and T_{e} in the plume. First, the results in Figs. 5(b) and 5(d) reveal a higher impact of plume size when the cathode is placed at larger radial positions: the axial profiles practically collapse for C3 cases, whereas the largest variations are found among C2 cases. Second, for any plume size, Figs. 5(b) and 5(d) show that ϕ and T_{e} along the channel midline increase with the radial position of the cathode (i.e., moving from C3 to C1 to C2). The plasma density, n_{e}, in the plume (not shown) is found to decrease from C3 to C1, and remain approximately constant from C1 to C2. Third, for case GP3C2, Fig. 4(a) reveals higher ϕ_{P} values near the axis and the midradius along the axial plume boundary, and lower values along the lateral plume boundary. This results in a higher radial electric field in the plume (not shown), which is the primary responsible for the higher plume divergence and velocity dispersion of C2 cases. The opposite behavior is found for case GP3C3, which shows lower and more uniform ϕ values at P, consistent with the lower plume divergence and velocity dispersion of C3 cases. Fig. 4(b) confirms the higher (lower) T_{e} values in the plume for C2 (C3) cases.

The trends with the cathode location found here for ϕ, T_{e}, and n_{e} in the near plume are well aligned with previous experimental works. Measurements in Ref. 3 for an externally-mounted cathode indicated that operating the thruster from a more distant cathode rather than a closer one yields higher ϕ and T_{e}, as well as lower n_{e} in the near plume. Sommerville *et al.*[7] showed that average values of ϕ and T_{e} in the near plume increase with the radial position of the externally-mounted cathode, particularly outside the MS, while average n_{e} values remained practically unchanged or decreased slightly. The authors noticed that higher ϕ values led to larger ion beam divergence due to the enhanced radial electric field. Plasma potential in the plume was also reported to increase when the externally-mounted cathode was placed outside the MS in Refs. 8 and 9, with the latter study reporting higher divergence. Compared to the operation with a centrally-mounted cathode, higher plasma potential in the plume was also observed for a 6 kW HET[2] when operating with an externally-mounted cathode.

Compared to C1 cases, the surface-averaged values of $e\phi_{\infty P}/T_{eP}$ over P are slightly lower for C3 cases ranging between 4.3 and 4.8 (with $T_{iP}/T_{eP} \approx 15$–20). The average value of T_{eP} is of about 0.7 eV, and the potential drop from P to infinity amounts to about 15% of the potential drop in the near plume downstream of $z/L_c = 3$. In contrast, C2 cases exhibit higher surface-averaged values of $e\phi_{\infty P}/T_{eP}$, ranging from 5.7 to 6.7, and lower values of $T_{iP}/T_{eP} \approx 5$. The trend of $e\phi_{\infty P}/T_{eP}$ with T_{iP}/T_{eP} found here is consistent with the simulation results for a MN reported in Ref. 43. The higher electron temperature in the plume for C2 cases, with average value of T_{eP} of about 3 eV increases the potential drop between P and infinity for these cases, which amounts to about 32% of the potential drop in the near plume downstream of $z/L_c = 3$, reaching up to 6% of V_d. The lack of a model for the anomalous cooling of magnetized electrons in the MN part of the near plume emerges as a more notable limitation in this scenario.

NOTE: explanation of behavior of ϕ_∞ (especially in C2 cases): The ratio $e\phi_{\infty P}/T_{eP}$, with $\phi_{\infty P} = \phi_P - \phi_\infty \geq 0$, is approximately constant with plume size, as expected in a sheath (for a dielectric wall with sonic ions this value is constant and depends on the elementary mass of the gas). The expected behavior is to have a constant value of ϕ_∞, and decreasing values of ϕ_P and T_{eP} with the plume size, so that $e\phi_{\infty P}/T_{eP} \simeq$ const. However, in our case, while ϕP decreases with plume size, T_{eP} remains constant (there is no cooling). Therefore, to keep $e\phi_{\infty P}/T_{eP} \simeq$ const., ϕ_∞ decreases with plume size.

V. CONCLUSION

Three major aspects of the numerical modelling of the near plume of a HET have been investigated in this work through the hybrid code HYPHEN. First, regarding boundary conditions imposed at the plume boundary P, a new GPC model, which enforces a net current-free condition at P, has been developed to overcome the limitations of the widely adopted LPC model, that imposes zero plasma current locally, i.e., at every point along the plume boundary. Second, the influence of plume size on the plasma solution, particularly on the electric current maps, have been assessed for both the GPC and LPC models. And third, the effects of the cathode location on the discharge performance and the coupling between cathode electrons and the ion beam have been investigated for externally-mounted cathodes, located inside (C1) and outside (C2) of the MS, and for a centrally-mounted cathode (C3).

For C1, the results for four plume sizes indicate that the GPC model provides a more robust plasma current solution against plume truncation. Differences in the plasma current between cases are primarily due to changes on the electron current. The GPC is found to limit electron detachment from magnetic lines induced by the plume boundary, providing an electron current solution that is more representative of the still magnetized electron population in the near plume region. In particular, the LPC yields a larger electron current towards the lateral plume boundary. This induces an increase in the electric potential on the order of the local electron temperature, and thus significant for near-plume diagnostics, and affects the dynamics of slow CEX ions, whose accurate characterization is central for assessing plume-satellite interaction effects.

For C2, the plasma current solution provided by the LPC is directly dependent on the plume size, making it unreliable. In this scenario, the GPC clearly outperforms the LPC: by locally decoupling ion and electron currents at P, it eliminates the artificial effects present on the electric current solution obtained with the LPC, providing a significantly more robust solution for different plume sizes, and thus increasing the reliability of the simulation results obtained for smaller, less computationally demanding plume domains. This fact is of central importance for comparison of simulation results with experimental data, which are mostly obtained in the plume.

Regardless of the cathode location, for a sufficiently large plume, changes on the coupling voltage with plume size are small relative to the discharge voltage. Therefore, the expansion of the main ion beam in the near plume and the thruster performance are minimally affected by plume size. Decreasing the cathode radial position (i.e., moving from C2 to C1 to C3), the discharge performance is enhanced: the cathode-beam coupling is improved, higher thrust and efficiency values are obtained and plume divergence and velocity dispersion is reduced. Furthermore, lower electric potential and electron temperature values, and higher plasma density values are found in the plume. These results are consistent with previous experimental and numerical results in the literature.

The values of ϕ_∞ are found to decrease monotonically with plume size for all cathode locations, with larger variations observed as the cathode radial position increases. These results suggest that simulating larger plumes are required to obtain a more precise estimation of ϕ_∞, and particularly when the cathode is located outside the MS.

No electron cooling is observed in the downstream MN-shaped region of the plume for any of the cases. The higher electron temperature observed in the plume for C2 cases increases the potential drop between P and infinity. These results highlight the need for a model to account for the experimentally observed cooling in HET plumes. Future efforts will concentrate on incorporating an anomalous electron cooling model, as the one proposed by Zhou *et al.* in Ref. 36, and on evaluating the new GPC model in scenarios representative of magnetically-shielded HETs with centrally-mounted cathodes, cylindrical HETs and electrodeless plasma thrusters with MN.

DATA AVAILABILITY STATEMENT

The data that support the findings of this study are available from the corresponding author upon reasonable request.

ACKNOWLEDGMENTS

This work has been supported by the CHEOPS LOW POWER project, funded by the European Union's Horizon 2020 Research and Innovation Program, under Grant Agreement number 101004331.

We thank Dr. Jesús Perales-Díaz for his active collaboration in the development of the numerical models and constructive comments.

Appendix A: Power balance and thrust efficiency

The plasma power balance for the steady state discharge is

$$P = P_P + P_{\mathrm{D}} + P_{\mathrm{A}} + P_{\mathrm{inel}}, \tag{A.1}$$

where: $P = I_{\mathrm{d}}V_{\mathrm{d}} + P_{\mathrm{C}}$ is the total power deposited into the plasma discharge, which is the sum of the discharge power, $P_{\mathrm{d}} = I_{\mathrm{d}}V_{\mathrm{d}}$, and the net power delivered through cathode electron emission, P_{C}, amounting to 1-2% of P; P_P is the plasma energy flow through P boundary; P_{D} and P_{A} are the power losses at the dielectric walls and at the anode wall, respectively; and P_{inel} corresponds to the power losses due to inelastic (e.g., ionization and excitation) collisions. All powers are defined as positive. The value of P_{inel} is obtained from a volumetric integral; P_P, is computed from the surface integral at the downstream plume boundary P (the integral of P''_{niP} and P''_{neP} yields the contribution of ions and electrons, respectively); and the values of P_{D} and P_{A} come from surface integrals at the respective walls.

The thrust efficiency is defined and factorized as

$$\eta = \frac{F^2}{2\dot{m}P} \equiv \eta_{\mathrm{ene}}\eta_{\mathrm{div}}\eta_{\mathrm{disp}}, \tag{A.2}$$

where the energy, divergence, and dispersion efficiencies are defined, respectively, as

$$\eta_{\mathrm{ene}} = \frac{P_{\mathrm{P}}}{P} \qquad \eta_{\mathrm{div}} = \frac{P_{\mathrm{zP}}}{P_{\mathrm{P}}}, \qquad \eta_{\mathrm{disp}} = \frac{F^2}{2\dot{m}P_{\mathrm{zP}}}, \tag{A.3}$$

with P_{zP} the flow of axial plasma energy across P. In Eq. (A.3), η_{ene} is a plasma source related efficiency that measures the relative power in the downstream plume, while plume-related efficiencies are η_{div}, which assesses the plume divergence based on axial energy and total energy flows, and η_{disp}, that quantifies the level of velocity dispersion of all plasma species (which would be one for a mono-velocity gas).

REFERENCES

[1] Tilley, D., de Grys, K., and Myers, R., "Hall thruster-cathode coupling," *35th Joint Propulsion Conference and Exhibit*, 1999, p. 2865.

[2] Jameson, K. K., Goebel, D. M., Hofer, R. R., and Watkins, R. M., "Cathode coupling in Hall thrusters," 30^{th} *International Electric Propulsion Conference*, No. IEPC-2007-278, Electric Rocket Propulsion Society, Fairview Park, OH, Florence, Italy, September 17–20, 2007.

[3] Beal, B. E., Gallimore, A. D., and Hargus Jr, W. A., "Effects of cathode configuration on Hall thruster cluster plume properties," *Journal of Propulsion and Power*, Vol. 23, No. 4, 2007, pp. 836–844.

[4] Hofer, R., Johnson, L., Goebel, D., and Wirz, R., "Effects of internally mounted cathodes on Hall thruster plume properties," *IEEE Transactions on Plasma Science*, Vol. 36, No. 5, 2008, pp. 2004–2014.

[5] McDonald, M. and Gallimore, A., "Cathode position and orientation effects on cathode coupling in a 6-kW Hall thruster," 31^{st} *International Electric Propulsion Conference*, No. IEPC-2009-113, Electric Rocket Propulsion Society, Fairview Park, OH, University of Michigan, Ann Arbor, MI, USA, September 20-24, 2009.

[6] Sommerville, J. and King, L., "Effect of cathode position on Hall-effect thruster performance and near-field plume properties," *44th AIAA/ASME/SAE/ASEE Joint Propulsion Conference & Exhibit*, No. AIAA-2008-4996, American Institute of Aeronautics and Astronautics, Reston, VA, Hartford, CT, USA, July 21-23, 2007.

[7] Sommerville, J. D. and King, L. B., "Hall-effect thruster–cathode coupling, part II: ion beam and near-field plume," *Journal of Propulsion and Power*, Vol. 27, No. 4, 2011, pp. 754–767.

[8] Turan, N., Kokal, U., Celik, M., and Kurt, H., "Experimental study of the effects of the cathode position and the electrical circuit configuration on the operation of HK40 Hall thruster and BUSTLab hollow cathode," *52nd AIAA/SAE/ASEE Joint Propulsion Conference*, No. AIAA-2016-4834, American Institute of Aeronautics and Astronautics, Reston, VA, Salt Lake City, UT, USA, July 25-27, 2016.

[9] Yu, D., Meng, T., Ning, Z., and Liu, H., "Confinement effect of cylindrical-separatrix-type magnetic field on the plume of magnetic focusing type Hall thruster," *Plasma Sources Science and Technology*, Vol. 26, No. 4, 2017, pp. 04LT02.

[10] Ding, Y., Li, H., Li, P., Jia, B., Wei, L., Su, H., Sun, H., Wang, L., and Yu, D., "Effect of relative position between cathode and magnetic separatrix on the discharge characteristic of Hall thrusters," *Vacuum*, Vol. 154, 2018, pp. 167–173.

[11] Frieman, J. D., King, S. T., Walker, M. L., Khayms, V., and King, D., "Role of a conducting vacuum chamber in the Hall effect thruster electrical circuit," *Journal of Propulsion and Power*, Vol. 30, No. 6, 2014, pp. 1471–1479.

[12] Frieman, J. D., Walker, J. A., Walker, M. L., Khayms, V., and King, D. Q., "Electrical facility effects on Hall thruster cathode coupling: Performance and plume properties," *Journal of Propulsion and Power*, Vol. 32, No. 1, 2016, pp. 251–264.

[13] Walker, J. A., Frieman, J. D., Walker, M. L., Khayms, V., King, D., and Peterson, P. Y., "Electrical facility effects on Hall-effect-thruster cathode coupling: discharge oscillations and facility coupling," *Journal of Propulsion and Power*, Vol. 32, No. 4, 2016, pp. 844–855.

[14]Walker, J. A., Langendorf, S. J., Walker, M. L., Khayms, V., King, D., and Pertson, P., "Electrical facility effects on Hall current thrusters: electron termination pathway manipulation," *Journal of Propulsion and Power*, Vol. 32, No. 6, 2016, pp. 1365–1377.

[15]Fife, J. M., *Hybrid-PIC modeling and electrostatic probe survey of Hall thrusters*, Ph.D. thesis, Massachusetts Institute of Technology, 1998.

[16]Hagelaar, G., Bareilles, J., Garrigues, L., and Boeuf, J., "Two-dimensional model of a stationary plasma thruster," *Journal of Applied Physics*, Vol. 91, No. 9, 2002, pp. 5592–5598.

[17]Parra, F. I., Ahedo, E., Fife, J. M., and Martínez-Sánchez, M., "A two-dimensional hybrid model of the Hall thruster discharge," *Journal of Applied Physics*, Vol. 100, No. 2, 2006, pp. 023304.

[18]Garrigues, L., Hagelaar, G., Boniface, C., and Boeuf, J., "Anomalous conductivity and secondary electron emission in Hall effect thrusters," *Journal of applied physics*, Vol. 100, No. 12, 2006, pp. 123301.

[19]Sommier, E., Scharfe, M., Gascon, N., Cappelli, M., and Fernandez, E., "Simulating plasma-induced Hall thruster wall erosion with a two-dimensional hybrid model," *Plasma Science, IEEE Transactions on*, Vol. 35, No. 5, 2007, pp. 1379–1387.

[20]Perales-Díaz, J., Domínguez-Vázquez, A., Fajardo, P., Ahedo, E., Faraji, F., Reza, M., and Andreussi, T., "Hybrid plasma simulations of a magnetically shielded Hall thruster," *Journal of Applied Physics*, Vol. 131, No. 10, 2022, pp. 103302.

[21]Cichocki, F., Domínguez-Vázquez, A., Merino, M., Fajardo, P., and Ahedo, E., "Three-dimensional neutralizer effects on a Hall-effect thruster near plume," *Acta Astronautica*, Vol. 187, 2021, pp. 498–510.

[22]Mikellides, I. and Katz, I., "Numerical simulations of Hall-effect plasma accelerators on a magnetic-field-aligned mesh," *Physical Review E*, Vol. 86, No. 4, 2012, pp. 046703.

[23]Keidar, M., Boyd, I. D., and Beilis, I. I., "Modeling of a high-power thruster with anode layer," *Physics of Plasmas*, Vol. 11, No. 4, 2004, pp. 1715–1722.

[24]Andreussi, T., Giannetti, V., Leporini, A., Saravia, M. M., and Andrenucci, M., "Influence of the magnetic field configuration on the plasma flow in Hall thrusters," *Plasma Phys. Control. Fusion*, Vol. 60, No. 1, 2018.

[25]Lopez Ortega, A. and Mikellides, I. G., "The importance of the cathode plume and its interactions with the ion beam in numerical simulations of Hall thrusters," *Physics of Plasmas*, Vol. 23, No. 4, 2016, pp. 043515.

[26]Mikellides, I. G., Katz, I., Hofer, R. R., and Goebel, D. M., "Hall-effect thruster simulations with 2-D electron transport and hydrodynamic ions," *31st International Electric Propulsion Conference*, paper 2009-114, Electric Rocket Propulsion Society, Fairview Park, OH, University of Michigan, Ann Arbor, MI, USA, 2009.

[27]Kubota, K., Cho, S., Watanabe, H., and Funaki, I., "Hybrid-PIC Simulation of Hall Thruster with Internally Mounted Cathode," *35th International Electric Propulsion Conference*, IEPC-2017-426, Atlanta, GA, USA, 2017.

[28]Cho, S., Kubota, K., Watanabe, H., Hara, K., and Funaki, I., "Comparing Internal and External Cathode Boundary Position in a Hall Thruster Particle Simulation," 35^{th} *International Electric Propulsion Conference*, No. IEPC-2017-402, Electric Rocket Propulsion Society, Fairview Park, OH, Georgia Institute of Technology, Atlanta, GA, USA, October 8-12, 2017.

[29]Cao, X., Liu, H., and Yu, D., "Simulation of discharge process of Hall thruster under the internal and external cathode conditions," *The European Physical Journal Applied Physics*, Vol. 90, No. 1, 2020, pp. 10801.

[30]Domínguez-Vázquez, A., *Axisymmetric simulation codes for Hall effect thrusters and plasma plumes*, Ph.D. thesis, Universidad Carlos III de Madrid, Leganés, Spain, 2019.

[31]Domínguez-Vázquez, A., Zhou, J., Fajardo, P., and Ahedo, E., "Analysis of the plasma discharge in a Hall thruster via a hybrid 2D code," 36^{th} *International Electric Propulsion Conference*, No. IEPC-2019-579, Electric Rocket Propulsion Society, Vienna, Austria, 2019.

[32]Duchemin, O., Rabin, J., Balika, L., Coduti, G., Vial, V., Vuglec, D., Cavelan, X., and Leroi, V., "Qualification Status of the PPS-5000 Hall Thruster Unit," 36^{th} *International Electric Propulsion Conference*, No. IEPC-2019-906, Electric Rocket Propulsion Society, Fairview Park, OH, 2019.

[33]Duchemin, O. B., Rabin, J., Coduti, G., and Le Méhauté, D., "Expanding the Mission Capture of the PPS® 5000 Hall Thruster," *ASCEND 2023*, 2023, p. 4790.

[34]Ahedo, E. and Merino, M., "Two-Dimensional Supersonic Plasma Acceleration in a Magnetic Nozzle," *Physics of Plasmas*, Vol. 17, No. 7, 2010, pp. 073501.

[35]Zhou, J., *Modeling and simulation of the plasma discharge in a radiofrequency thruster*, Ph.D. thesis, Universidad Carlos III de Madrid, Leganés, Spain, 2021.

[36]Zhou, J., Domínguez-Vázquez, A., Fajardo, P., and Ahedo, E., "Magnetized fluid electron model within a two-dimensional hybrid simulation code for electrodeless plasma thrusters," *Plasma Sources Science and Technology*, Vol. 31, No. 4, 2022, pp. 045021.

[37]Pérez-Grande, D., González-Martínez, O., Fajardo, P., and Ahedo, E., "Analysis of the numerical diffusion in anisotropic mediums: benchmarks for magnetic field aligned meshes in space propulsion simulations," *Applied Sciences*, Vol. 6, No. 11, 2016, pp. 354.

[38]Ahedo, E. and Pablo, V., "Combined effects of electron partial thermalization and secondary emission in Hall thruster discharges," *Physics of Plasmas*, Vol. 14, 2007, pp. 083501.

[39]Lam, C. M., Fernandez, E., and Cappelli, M. A., "A 2-D hybrid Hall thruster simulation that resolves the ExB electron drift direction," *IEEE Transactions on Plasma Science*, Vol. 43, 2015, pp. 86–94.

[40]Marks, T. A., Mikellides, I. G., Lopez Ortega, A., and Jorns, B., "Hall2De Simulations of a Magnetic Nozzle," *AIAA Propulsion and Energy 2020 Forum*, AIAA 2020-3642, 2020.

[41]Merino, M. and Ahedo, E., "Plasma detachment in a propulsive magnetic nozzle via ion demagnetization," *Plasma Sources Science and Technology*, Vol. 23, No. 3, 2014, pp. 032001.

[42]Jorns, B. A. and Byrne, M. P., "Model for the dependence of cathode voltage in a Hall thruster on facility pressure," *Plasma Sources Science and Technology*, Vol. 30, No. 1, 2021, pp. 18.

[43]Ahedo, E., Correyero, S., Navarro, J., and Merino, M., "Macroscopic and parametric study of a kinetic plasma expansion in a paraxial magnetic nozzle," *Plasma Sources Science and Technology*, Vol. 29, No. 4, 2020, pp. 045017.

[44]Zhou, J., Sánchez-Arriaga, G., and Ahedo, E., "Time-dependent expansion of a weakly-collisional plasma beam in a paraxial magnetic nozzle," *Plasma Sources Science and Technology*, Vol. 30, No. 4, 2021, pp. 045009.